coatings

MDPI

*Article*

# The Role of Anodising Parameters in the Performance of Bare and Coated Aerospace Anodic Oxide Films

**Mariana Paz Martinez-Viademonte [1,2,*], Shoshan T. Abrahami [3], Meisam D. Havigh [1], Kristof Marcoen [1], Theodor Hack [2], Malte Burchardt [4] and Herman Terryn [1]**

[1] Research Group, Electrochemical and Surface Engineering (SURF), Department of Materials and Chemistry, Vrije Universiteit Brussel, Pleinlaan 2, 1050 Brussels, Belgium; meisam.dabiri.havigh@vub.be (M.D.H.); kristof.marcoen@vub.be (K.M.); herman.terryn@vub.be (H.T.)
[2] Airbus Central Research and Technology, Willy-Messerschmitt-Straße 1, 82024 Taufkirchen, Germany; theo.hack@airbus.com
[3] Department of Materials Science and Engineering, Delft University of Technology, Mekelweg 2, 2628 CD Delft, The Netherlands; s.t.abrahami@tudelft.nl
[4] Airbus Operations GmbH Deutschland, Airbus Allee 1, 28199 Bremen, Germany; malte.burchardt@airbus.com
* Correspondence: mariana.paz@airbus.com

**Abstract:** The anodising process parameters (voltage, temperature, and electrolyte) control the morphology and the chemical composition of the resulting anodic oxide film by altering the balance between oxide growth and oxide dissolution reactions. The porosity of the oxide film is reduced by the addition of tartaric acid to a sulfuric acid electrolyte, while anodising at elevated temperatures enhances oxide dissolution, leading to wider pores and rougher surfaces. No significant changes in the oxide chemical composition as a function of anodising parameters was found; in particular, no tartrate incorporation took place. The resistance of uncoated anodic oxide films against aggressive media and galvanic stress as a function of anodising parameters has been studied by electrochemical methods. Anodising in a mixed tartaric and sulfuric acid electrolyte improves the resistance of the anodic oxide against galvanic stress and aggressive media in comparison to sulfuric acid anodising processes. However, the corrosion protection performance of the anodic oxide films in combination with a corrosion-inhibitor loaded organic coating is not governed by the blank oxide properties but by the adhesion-enhancing morphological features formed during anodising at elevated temperatures at the oxide/coating interface.

**Keywords:** anodising; AA2024; tartaric-sulphuric acid; pitting corrosion



**Citation:** Paz Martinez-Viademonte, M.; Abrahami, S.T.; Havigh, M.D.; Marcoen, K.; Hack, T.; Burchardt, M.; Terryn, H. The Role of Anodising Parameters in the Performance of Bare and Coated Aerospace Anodic Oxide Films. *Coatings* **2022**, *12*, 908. https://doi.org/10.3390/coatings12070908

Academic Editor: Xiao Han

Received: 30 May 2022
Accepted: 24 June 2022
Published: 27 June 2022



## 1. Introduction

Lightweight materials with high specific mechanical properties are the preferred choice for aerospace applications. Among the most commonly used materials are aluminium alloys from the 2xxx (Al-Cu) and 7xxx (Al-Cu-Zn-Mg) series alloys [1]. While the alloying elements endow outstanding mechanical properties to the alloy, they are detrimental to corrosion properties. The second phases present, enriched in alloying elements, lead to the formation of micro-galvanic coupling with the aluminium matrix [2–5]. As a consequence, these alloys are particularly sensitive to localised corrosion [6,7]. Adding to that intrinsic sensitivity, aerospace products typically experience varying environmental conditions during their long service life (in the range of 30 years) that are demanding in terms of corrosion prevention such as the exposure to aggressive media and environments and the galvanic stress induced by multi-material assembles (e.g., with stainless steel or carbon fibre reinforced plastics). To overcome these challenging boundary conditions, a reliable corrosion protection system must be designed.

While there are other possible technologies and configurations that could be used (e.g., chemical conversion coatings [8], sol-gel [9], or plasma electrolytic oxidation (PEO)

coatings [10]), a typical corrosion protection scheme for aerospace applications consist of numerous layers: a clad layer, a porous anodic oxide film, an organic coating loaded with corrosion inhibitors, and an organic topcoat. This is schematically depicted in Figure 1. In particular, the anodic oxide film is formed by an electrochemical process (anodising) by which the oxide film on the aluminium surface is artificially thickened. The natural oxide film present on aluminium is in the range of a few nanometres thick, whereas the oxide film resulting from an anodising process can reach thicknesses of several micrometres. When the aluminium oxide film is soluble in the anodising electrolyte, a competition between the oxide growth and oxide dissolution reactions takes place, and a porous oxide morphology develops [11]. Despite the porous nature of the oxide film, a continuous thin (in the nanometres range) barrier layer of scalloped morphology is formed during the first instants of anodising. The thickness of the barrier layer is proportional to the voltage imposed during the anodising process and remains constant throughout the process [12]. The barrier layer thickness is limited by the maximum thickness at which continuous ionic flow takes place [11]. Should the barrier layer become thicker, the oxide formation reaction would stop, whilst the oxide dissolution reaction at the pore bottom would still take place. By these means, the barrier layer would become thinner until the ionic flow is re-established and oxide growth resumes [13,14]. Once the barrier layer has formed, pore nucleation takes place, and stable pore growth starts [12].

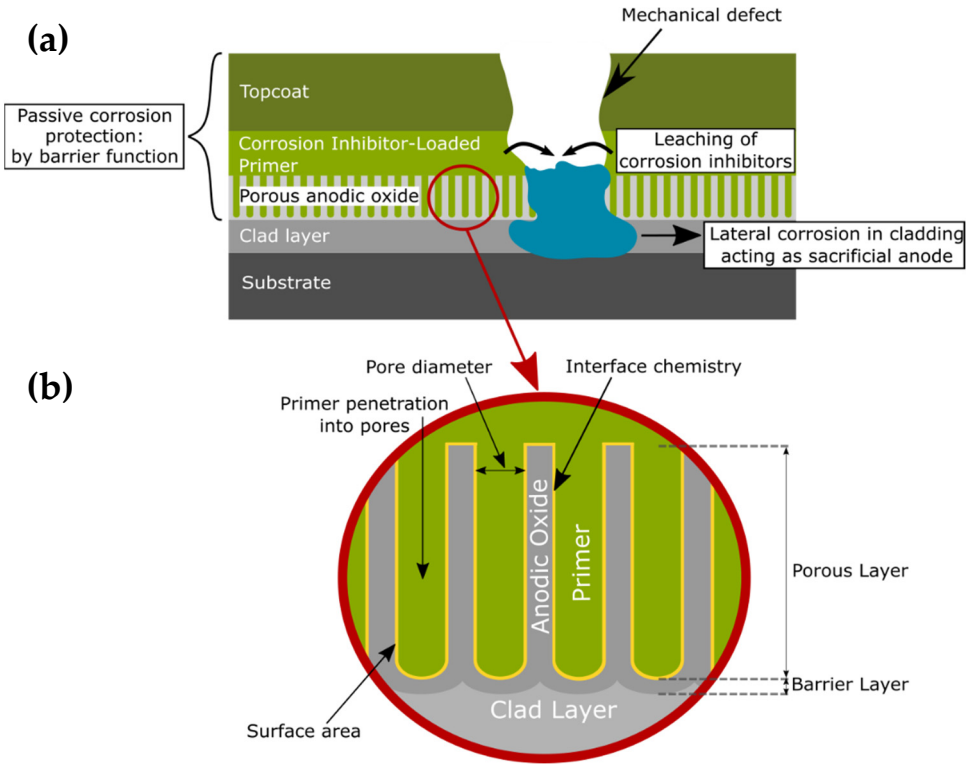


**Figure 1.** Schematic illustration of (**a**) typical corrosion protection scheme in aerospace applications and (**b**) important features of corrosion protective anodic oxide films. Reprinted with permission from [15].

The morphology and, to some extent, the chemical composition of the anodic oxide film can be controlled by altering the balance between oxide growth and oxide dissolution reactions. This can be done through anodising process parameters such as the formation voltage (or current), the nature and chemical composition of the anodising electrolyte, and the electrolyte temperature. The thickness of the barrier layer, the size of the pore cell, and the oxide growth rate can be influenced by the imposed formation voltage, with higher voltages leading to thicker barrier layers, bigger pore cells, and faster growth rates [11,12,14]. The nature of the electrolyte, mainly its ability to dissolve the oxide film,

determines the formation of a barrier or a porous oxide film [11,12]. The aggressiveness of the electrolyte towards the oxide influences the dissolution rate, and its conductivity affects the oxide growth rate. In addition, a species present in the electrolyte can be incorporated into the oxide film, and the electrolyte chemical composition influences the chemistry of the resulting oxide [11,16,17]. Finally, an increase in the electrolyte temperature translates into an increase in both the oxide growth and oxide dissolution reaction rates. The enhanced oxide dissolution reaction is particularly interesting from a morphological perspective, as it leads to a widening of the pore mouths at the oxide/electrolyte interface [18].

The function of the porous anodic oxide film in aerospace corrosion protection systems is two-fold. On the one hand, it provides passive corrosion protection due to its nearly inert properties (in neutral pH). On the other hand, its porous morphology enhances the adhesion of the corrosion-inhibitor loaded organic coating, as it improves mechanical interlocking [19] and the number of physical–chemical interactions at the interface [17] through the penetration of the coating into the intricate porosity. Considering the influence of anodising parameters on the anodic oxide film morphology and surface chemistry, it is clear that anodising parameters also play a key role in the performance of the anodic oxide film in terms of barrier corrosion protection and adhesion enhancement.

While the standard anodising procedure in the aerospace industry in the past consisted of chromic acid anodising (CAA), in the last two decades, alternative processes have been developed due to the restrictions imposed on hexavalent chromium for its toxicity [20,21]. Among them, an anodising process using a mixed tartaric-sulfuric acid electrolyte (TSA) was introduced [22]. It was shown that the addition of tartaric acid improves corrosion protection compared to sulfuric acid anodising (SAA) [23–32], even though the exact mechanism by which the addition of tartaric acid leads to better corrosion protection properties has not been fully understood.

The present work studies the effect of anodising parameters (voltage, temperature, and tartaric acid concentration) on the morphological features, surface chemistry stability, and corrosion resistance of bare and coated anodic oxide films. The interrelations linking the anodising parameters to the oxide properties, the oxide corrosion protection, and adhesion performance are highlighted and discussed.

## 2. Materials and Methods

### 2.1. Pre-Treatment

The test panels are made of an AA2024 alloy cladded with a commercially pure aluminium grade according to WL 3.1364-1. The panels have been degreased in an alkaline cleaner for 15 min at 60 °C. Subsequently, alkaline etching for 1 min at 60 °C was performed. Finally, the panels have been desmutted in a fluoride containing acidic pickling solution for 5 min at 35 °C. Between each of these pre-treatment steps (degreasing, etching and pickling), the panels have been rinsed in agitated deionised water at room temperature for three minutes.

### 2.2. Anodising

Anodising has been carried out in three electrolytes: sulfuric acid electrolyte (SAA, 40 g/L sulfuric acid) and two mixed tartaric-sulfuric acid electrolytes with 40 g/L sulfuric acid and two different concentrations of tartaric acid (TSA, 80 g/L tartaric acid; $T^{+}$SA, 150 g/L tartaric acid). The composition of the three anodising electrolytes was selected in line with literature on this subject [23,28,30]. After a voltage ramp of 1 min, the panels have been anodised at a constant potential. Two anodising voltages have been used: 14 V and 20 V. In addition, the temperature of the anodising electrolyte has been varied, ranging from 37 °C to 55 °C.

The applied anodising conditions are listed in Table 1. The anodising time has been adjusted to target a total layer thickness of 4 µm based on previous results [33].

**Table 1.** Anodising conditions.

| Electrolyte | Voltage [V] | Temperature [°C] | Time at Constant V [min] |
|---|---|---|---|
| SAA | 14 | 45 | 10 |
| | 20 | 37 | 8 |
| TSA | 14 | 55 | 8 |
| | 20 | 37 | 9 |
| $T^{+}SA$ | 14 | 55 | 10 |
| | 20 | 37 | 10 |

Barrier anodic oxide films have been prepared to assess the chemical composition of the surface of the resulting oxide. To create this type of films, electropolished 40 mm × 40 mm × 1.2 mm panels were degreased in isopropanol, immersed in an alkaline etching solution at 60 °C for 15 s and in an acidic pickling solution at 35 °C for 1 min; then, the panels were galvanostatically anodised at 20 mA/cm$^2$ for 5 s. In this way, the anodising process is stopped before the pores start forming, resulting in a thin barrier oxide film. This barrier–layer approach has been previously employed in the work of Abrahami et al. [17].

### 2.3. Organic Coating Application

Some of the panels have been coated with an organic coating to assess the corrosion protection performance of painted samples and to study the influence of the anodising parameters on the adhesion properties.

A Cr(VI)-free inhibited solvent-based epoxy model primer was applied to the samples by spraying targeting a coating thickness of 20 µm (±5 µm).

A compatible epoxy topcoat layer was applied on the panels intended for the filiform corrosion (FFT) experiment on top of the model primer, targeting a coating thickness of 25 µm (±5 µm).

### 2.4. Field Emission Scanning Electron Microscopy (FE-SEM)

The morphology of the test panels has been characterised by a Zeiss Auriga field emission scanning electron microscope (Jena, Germany) with an accelerating voltage of 15 kV. The anodic oxide films have been observed in top and cross-section view. All samples were sputtered with platinum (2 nm) to avoid charging effects. The samples for cross-section observation were obtained by fracturing the substrate at room temperature. The quantitative assessment of the micrographs has been conducted with the aid of an open source image analysis software (ImageJ).

### 2.5. X-ray Photoelectron Spectroscopy (XPS)

XPS analysis has been conducted using a PHI Versaprobe III (Physical Electronics, Chanhassen, MN, USA) device equipped with an Al Kα monochromatic X-Ray source. The aim of this analysis was to characterise the chemical composition of the anodic oxide films. A survey scan of the surface of both porous and barrier anodic oxides has been performed at a take-off angle of 45°, a spot size of 100 µm, with a pass energy of 280 eV and a step size of 1 eV.

### 2.6. Chronoamperometry

The pitting potential of the non-anodised substrate material has been determined by applying a constant current (200 µA/cm$^2$) for two hours, using a 3.5 wt.% NaCl electrolyte in a three-electrode setup (3 M KCl Ag/AgCl as reference electrode and a platinum counter electrode). The potential has been tracked, and the constant value reached after the two hours measurement has been taken as the pitting potential. The pitting potential has been measured three times to ensure repeatability. The anodised substrates have been polarised at a potential slightly above the pitting potential of the substrate ($E_{pit}$ + 50 mV) in a 3.5 wt.%

NaCl. The time to reach two current density thresholds, associated with pit initiation and metastable pitting (20 μA/cm$^2$) and stable pit growth (150 μA/cm$^2$), is monitored.

This approach has been previously proposed by Vignoli et al. [24] to study the resistance of anodic oxide films to pitting corrosion. This method allows to quantitatively evaluate the susceptibility to pitting of different anodic oxides by quantifying the time under polarisation until a rise in current density, up to the two defined thresholds, takes place. The rise in current density is first associated with interfacial reactions and transport mechanisms and, at a later stage, to pit initiation, metastable pitting, and stable pit growth at the oxide/metal interface. The two current density thresholds considered for the assessment of the susceptibility to pitting corrosion are associated to pit initiation and stable pit growth. The pitting mechanism that leads to the current density increase is schematically depicted in Figure 2, based on the work by McCafferty [34]. Figure 2, however, does not take into account the presence of impurities (residual intermetallics) in the clad layer or oxide defects. Oxidation of these impurities can play a significant role on the pit initiation and pit growth, while defect areas act as weak spots in which pitting will take place earlier and preferentially.

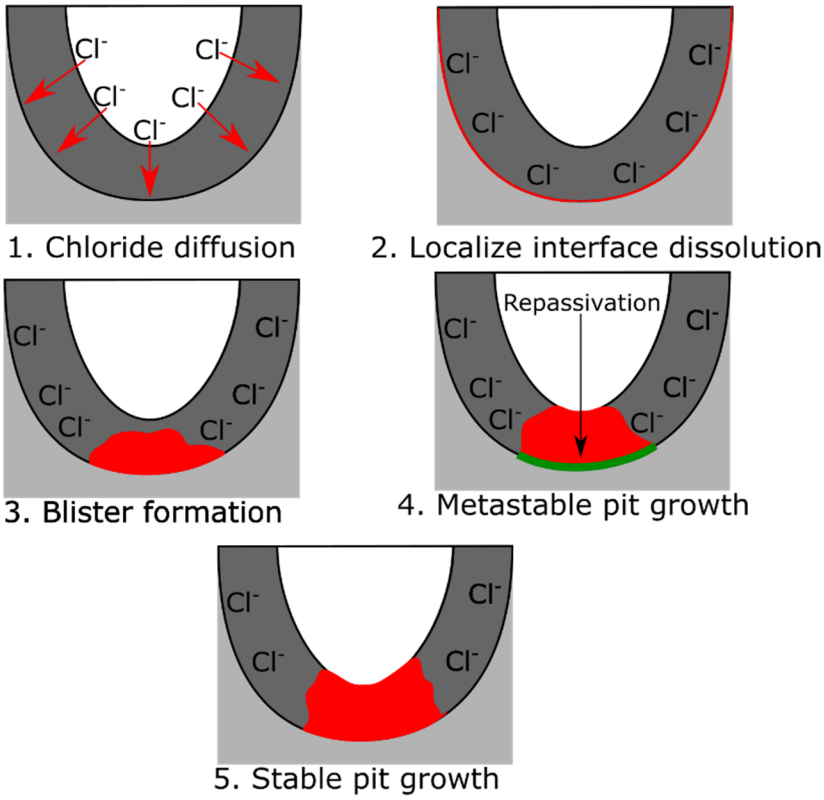


**Figure 2.** Schematic illustration of the pitting corrosion mechanism of anodic oxide films on aluminium substrates based on the work by McCafferty [34].

From the experimental parameters proposed by Vignoli et al. [24], the electrolyte NaCl concentration (from 0.6 wt.% to 3.5 wt.%) and potential gap (from $E_{pit}$ + 30 mV to $E_{pit}$ + 50 mV) have been varied, with the aim of increasing the overall aggressiveness of the experiment.

### *2.7. Odd Random Phase-Electrochemical Impedance Spectroscopy (ORP-EIS)*

Odd random phase electrochemical impedance spectroscopy (ORP-EIS) is a multi-sine time-resolved electrochemical impedance spectroscopy technique that allows to obtain a better time resolution of non-stationary electrochemical processes compared to classical single-sine EIS. During a conventional impedance measurement of a non-stationary process,

the condition of the measured system would change from the first excitation signal at high frequencies to the last excitation signal at low frequencies; a multi-sine technique allows to obtain a snapshot of the non-stationary process at a given point in time.

The excitation signal used for ORP-EIS measurements consists of several harmonically coupled sine waves. Only odd harmonics are perturbed. Moreover, in a group of three consecutive odd harmonics, one of them is randomly omitted while the other two are excited. All the harmonically related waves that form the final excitation signal are of equal amplitude (10 mV RMS around the open circuit potential). The phase of each of these sine waves is randomly assigned.

The response of the system to the excitation signal is recorded in both excited and non-excited frequencies. An insight into non-linear and non-stationary behaviour of the system under study can be gained by analysing the response of the system in the non-excited frequencies. This methodology has been thoroughly discussed elsewhere [35–38].

In this work, ORP-EIS experiments have been carried out to characterise the degradation behaviour of anodic oxide films in aggressive acidic and alkaline solutions. For this purpose, the oxide films were exposed to an acidified (pH 3 adjusted by the addition of HCl) and to an alkalised (pH 10 adjusted by the addition of NaOH) bulk dilute Harrison's solution (0.5 g/L NaCl and 3.5 g/L $(NH_4)_2SO_4$). The dilute Harrison's solution is a well-known corrosive solution commonly used to study the degradation of protective coatings and the corrosion rate of metals. A three-electrode setup has been used, which consisted of an Ag/AgCl reference electrode, a platinum counter electrode, and the sample itself as a working electrode. After every 1200 s of immersion, an impedance spectrum between 0.01 and $10^4$ Hz was obtained.

### *2.8. Corrosion Testing: Neutral Salt Spray (NSST)*

To study corrosion in the presence of a physical defect, coated test panels have been artificially damaged using two crossing u-shaped scribes forming an X on the panel surface. The scribes are 1 mm wide and have a depth between 200 µm and 300 µm, ensuring that the damage penetrates through the paint, oxide, and cladding, thus reaching the substrate alloy. This procedure is defined in the ISO 17872 [39] standard and is shown in Figure 3. The scribes have been created by a rotating saw.

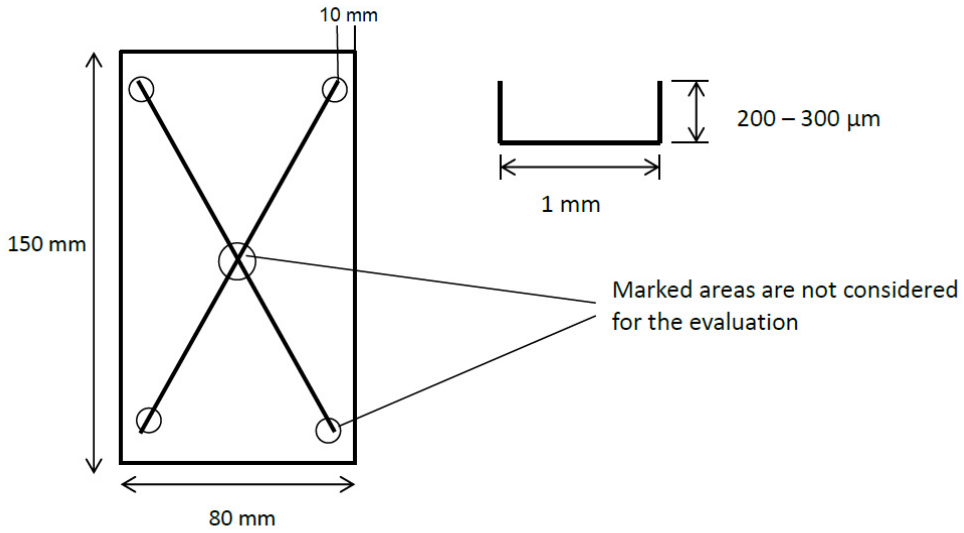


**Figure 3.** Description of the artificial damage described in ISO 17872 [39] and applied on the painted panels for NSST and FFT.

Shortly after scribing, the panels have been transferred to a neutral salt spray test chamber according to ISO 9227 [40] for 3000 h. A visual inspection was carried out after 168, 336, 500, 1000, 2000, and 3000 h. In this inspection, attention is given to changes in the scribe colour (tarnishing), the appearance of pits, the presence of corrosion products, paint

discoloration, and the length of the paint creepage, which is measured starting from the artificial defect.

### 2.9. Corrosion Testing: Filiform Corrosion (FFT)

The ability of the corrosion protection scheme (anodic oxide film + primer + topcoat) to prevent filiform corrosion has been studied according to the EN3665 [41] standard. For this purpose, test panels have been scribed according to ISO 17872 [39] in the same way as for the NSST panels.

Shortly after scribing, the panels were pre-exposed to hydrochloric acid vapour for one hour. The samples were then transferred to a cabinet at 40 °C and 82% relative humidity for 1000 h. Visual inspections were carried out after 168, 336, 500, 750 and 1000 h. In each of these inspections, the lengths of the 5 longest filaments were noted. After the test, some selected specimens have been automatically assessed by a Schäfter + Kirchhoff (Hamburg, Germany) corrosion inspector scanner and the associated automatic image processing software to further increase the statistical relevance of the obtained results.

### 2.10. Adhesion Testing: Cross-Cut Test

Adhesion performance was assessed using ISO 2409 [42] standard for the cross-cut adhesion between a substrate and organic coating. First, the thickness of the coating was measured by eddy current. Then, six parallel cuts, at a distance of 1 mm from each other, are performed in two perpendicular directions, forming a lattice. In this particular case, the cuts were made by a motor-driven single blade at a constant force. The force applied was chosen to ensure complete penetration of the cutting blade through the organic coating. The lattice area is softly cleaned with a brush to remove any coating debris and a pressure sensitive tape (TESA 4651, Norderstedt, Germany) is applied, covering the lattice (test area). The tape is rapidly removed, and the visual appearance of the test area is assessed according to the grading system described in the ISO 2409 standard [42]. In order to assess the adhesion stability of the coating in the presence of moisture, the test has been conducted on dry samples, as well as on samples that were immersed in deionised water for two weeks.

## 3. Results

### 3.1. Anodic Oxide Film Characterisation

#### 3.1.1. Oxide Morphology

Figures 4 and 5 show micrographs of the anodic oxide films obtained for all investigated parameter combinations in top view and in cross-section, respectively.

The anodic films formed in an electrolyte at elevated temperatures (at 45 °C or 55 °C; see images (a), (c), and (e) in Figures 4 and 5) present a rougher surface and thinner pore walls compared to the flatter and smoother oxides obtained at 37 °C (images (b), (d), and (f) in Figures 4 and 5). In addition, it can be observed, especially in images (b), (d), and (f) in Figures 4 and 5, that the addition of tartaric acid leads to a reduced oxide porosity, especially at the surface of the anodic oxide.

Table 2 summarizes key morphological features derived from the FE-SEM images. The oxide layer thickness has been measured in cross-section. The average oxide layer thickness ranges between 4.16 and 4.75 µm for all samples. The morphology of the pores has been analyzed from top view images aided by automated image analysis software. The statistical results obtained from the automated image analysis show average pore mouth diameter and pore densities for the high temperature anodising processes' conditions, which double and triple, respectively, that of the lower temperature anodising electrolyte.

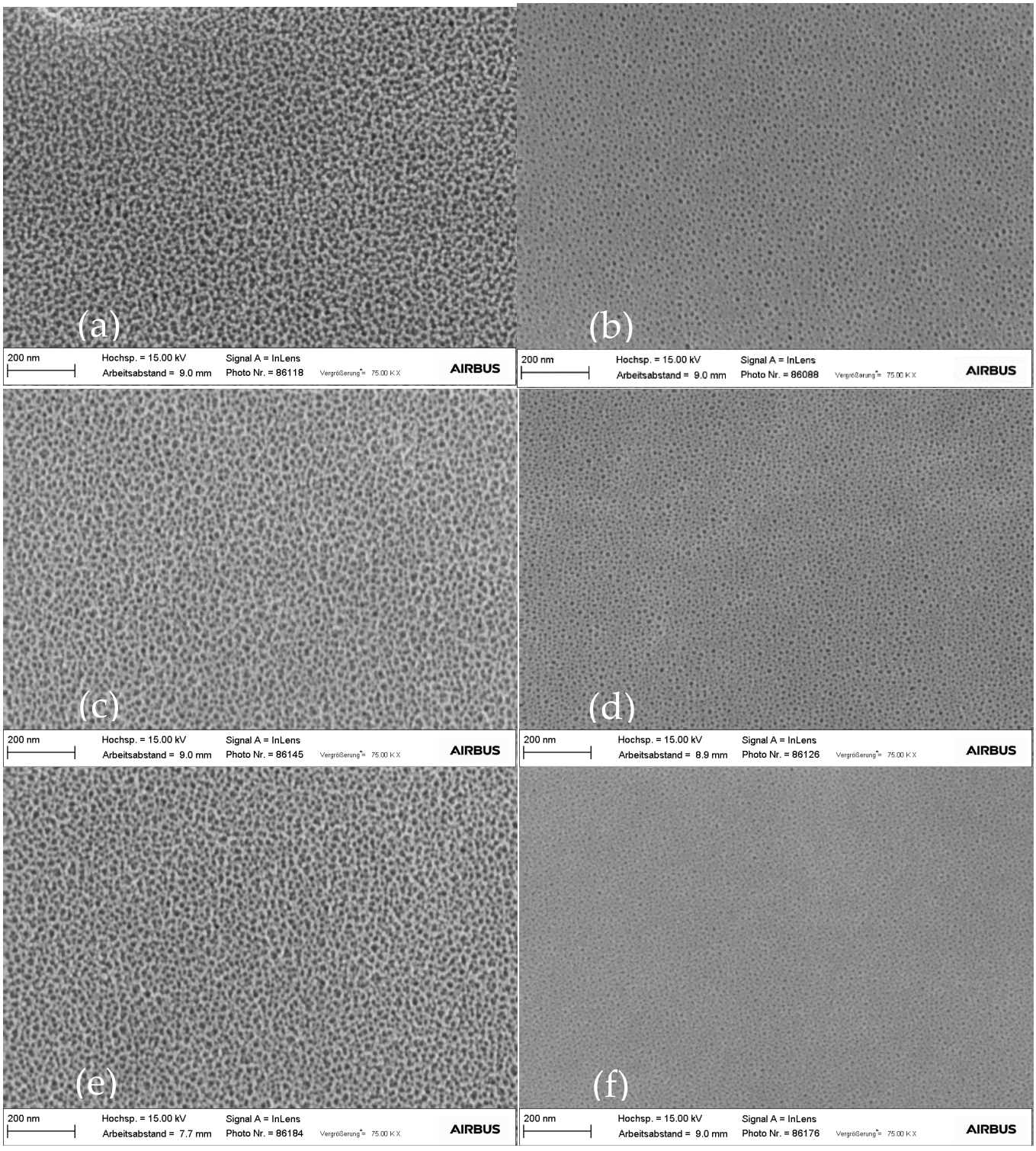


**Figure 4.** FE-SEM micrographs in top view of (**a**) SAA 14 V 45 °C; (**b**) SAA 20 V 37 °C; (**c**) TSA 14 V 55 °C; (**d**) TSA 20 V 37 °C; (**e**) $T^{+}$SA 14 V 55 °C; (**f**) $T^{+}$SA 20 V 37 °C.

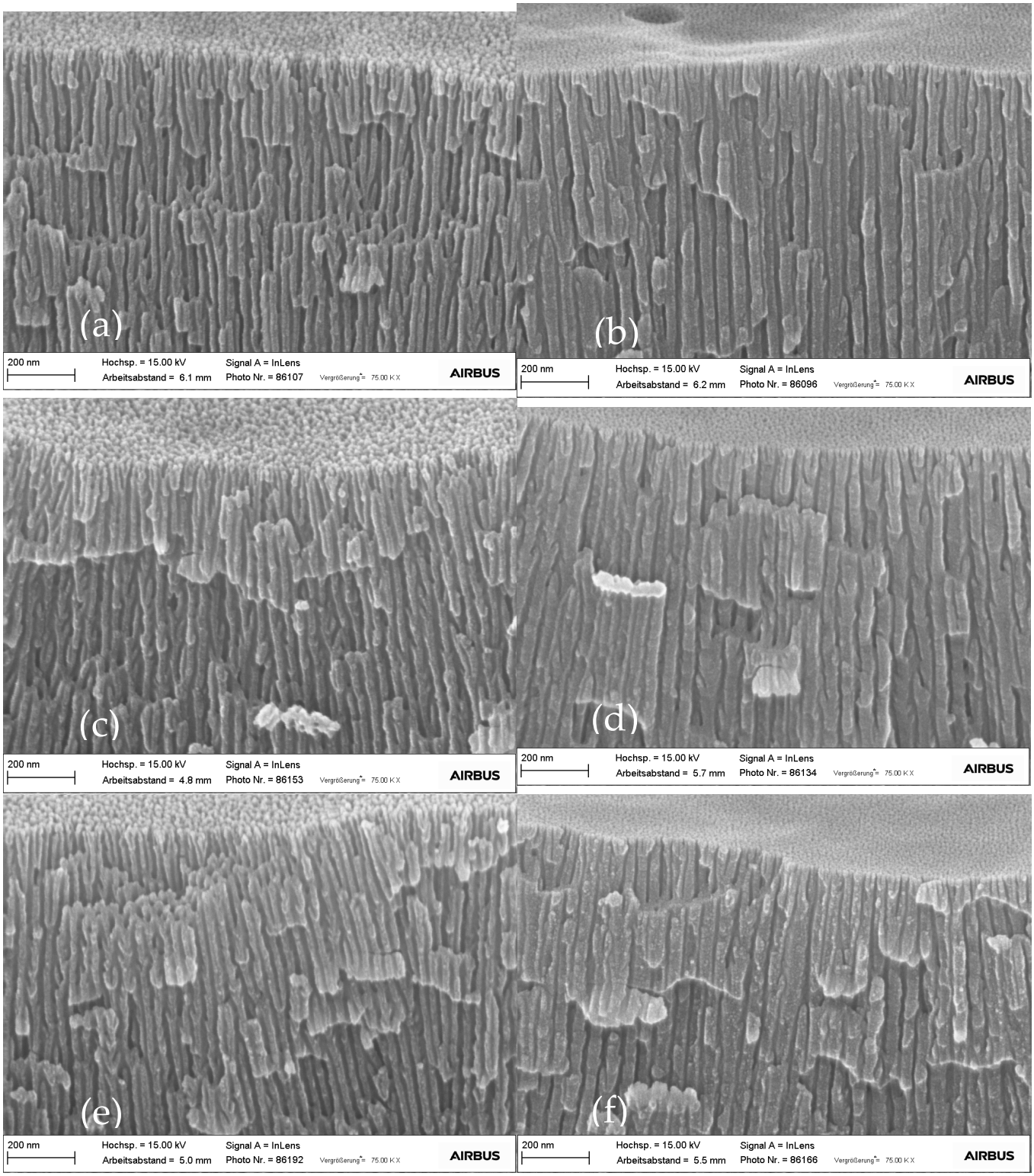


**Figure 5.** FE-SEM micrographs in cross-section of (**a**) SAA 14 V 45 °C; (**b**) SAA 20 V 37 °C; (**c**) TSA 14 V 55 °C; (**d**) TSA 20 V 37 °C; (**e**) $T^{+}$SA 14 V 55 °C; (**f**) $T^{+}$SA 20 V 37 °C.

**Table 2.** Summary of morphological features measured from FE-SEM imaging.

| Oxide | Thickness | SD | Avg. Pore Mouth ø | SD Avg. Pore Mouth ø | Pore Density | Porosity |
|---|---|---|---|---|---|---|
| Units | µm | µm | nm | nm | Pores/µm$^2$ | Area % |
| SAA 14 V 45 °C | 4.16 | 0.02 | 17.3 | 6.2 | 1201.7 | 34.3 |
| SAA 20 V 37 °C | 4.75 | 0.01 | 9.4 | 2.5 | 3095.6 | 7.0 |
| TSA 14 V 55 °C | 4.45 | 0.05 | 19.6 | 6.9 | 1113.7 | 22.1 |
| TSA 20 V 37 °C | 4.26 | 0.05 | 9.1 | 2.7 | 3518.3 | 5.8 |
| T$^+$SA 14 V 55 °C | 4.57 | 0.08 | 20.2 | 7.3 | 1047 | 23 |
| T$^+$SA 20 V 37 °C | 4.62 | 0.03 | 8 | 2.5 | 3913.6 | 6.7 |

### 3.1.2. Oxide Chemical Composition

The chemical composition of the oxide films has been studied by means of XPS. Although the study of porous anodic oxide films is interesting, as they are identical to the ones ultimately used for corrosion protection of aerospace structures, its porous nature leads to an uncontrolled mixed information signal and charging effects, which can come from the top surface, but also from the interior of the porous structures. Therefore, the results obtained from the characterisation of such porous films are qualitatively relevant; however, such data cannot be reliably quantified. To overcome this difficulty, barrier anodic oxide films have also been studied. Quantitative results are available in the Supplementary Materials.

The XPS survey scans of barrier anodic oxide films, obtained at a 45° take off angle (Figure 6), yield very similar spectra for all six oxides. In all cases, signals corresponding to oxygen, aluminium, carbon, sulfur, and fluoride are detected. In addition, in some of the points measured, a small sodium signal is detected. The presence of sodium originates most likely from contamination that took place during surface preparation.

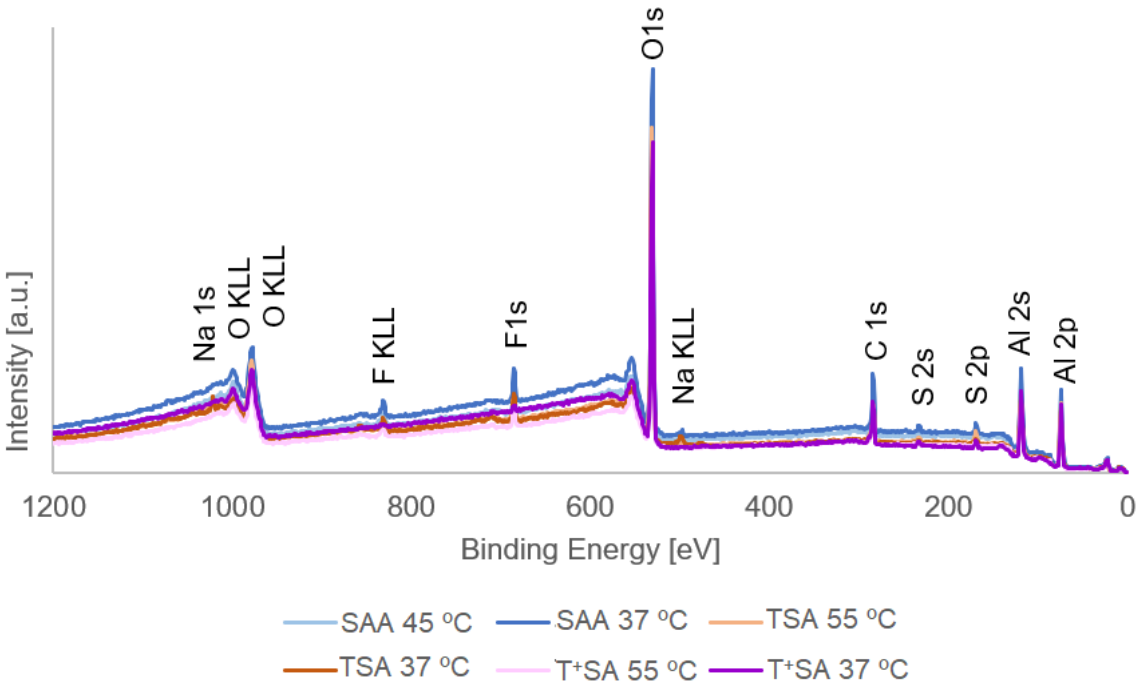


**Figure 6.** XPS survey scans of the six barrier anodic oxide films under study.

The longer exposure to the anodising electrolyte, as well as the morphology of porous anodic oxide films, can lead to differences in the chemical composition of the porous oxide compared to the barrier oxide films previously studied. For this reason, the chemical composition of porous oxide films obtained from anodising using the different conditions mentioned in Table 1 has been studied as well. The XPS spectra resulting from the survey

scan is very similar for all six oxides under consideration. Figure 7 shows, similar to the barrier oxide films, the presence of oxygen, aluminium, carbon, sulfur, and fluoride.

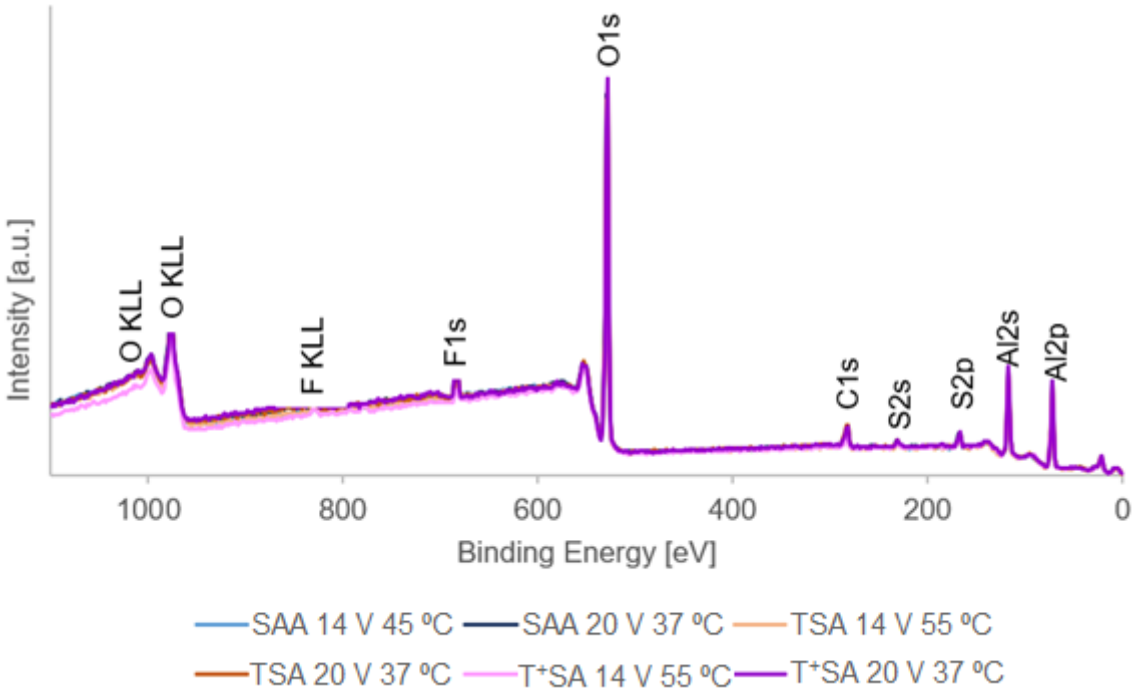


**Figure 7.** XPS survey scans of the six porous anodic oxide films under study.

More detailed characterisation of the oxide chemistry by XPS and by time of flight secondary ion mass spectroscopy (ToF-SIMS) can be found in the Supplementary Materials.

### *3.2. Protective Behaviour of Anodic Oxide Films*

#### 3.2.1. Chronoamperometry

Figure 8 shows the evolution of current density during the polarisation at 50 mV above the pitting potential of the substrate alloy. The polarisation experiments at 50 mV above the pitting potential were replicated, obtaining comparable results. For better visualisation, only one set of results is shown in Figure 8.

SAA oxide films formed at elevated temperature and lower voltage (45 °C, 14 V) show the earliest (<1 h) increase in current density compared to the rest of the oxides. In the case of the SAA oxide anodised at 37 °C and 20 V, the polarisation time to reach a steady current density increase is approximately 1 h. For TSA oxides, a significant current rise also takes place after a polarisation time in the order of magnitude of 1 h. However, the surface of the SAA oxide seems to be more active, as indicated by the marked and sharp current density peaks throughout the measurement time. Finally, the $T^+$SA anodic oxides show a significantly longer stability period (ca. 10 h) until a significant increase in current density takes place. Moreover, for $T^+$SA, similar to what was observed for SAA oxides, the combination of higher voltage (20 V) and lower anodising temperature (37 °C) yields the longest stability period.

To ease a more quantitative comparison among oxides, two current density thresholds have been defined and marked in red in Figure 8. The two thresholds are 20 $\mu A/cm^2$, associated to pit initiation and metastable pitting [24], and 150 $\mu A/cm^2$, associated to stable pit growth. To minimise the influence of noise in the measurement, it is considered that a threshold is met if five consecutive measurement points (or five consecutive seconds) are at or above the defined threshold. The addition of 80 g/l of tartaric acid to the SAA electrolyte (TSA) delays the initiation of pitting, whereas the time to stable pit growth is similar to that observed for SAA oxides anodised at 20 V and 37 °C. Further addition of

tartaric acid, up to 150 g/l ($T^+SA$), substantially increases the time of both pit initiation and stable pit growth.

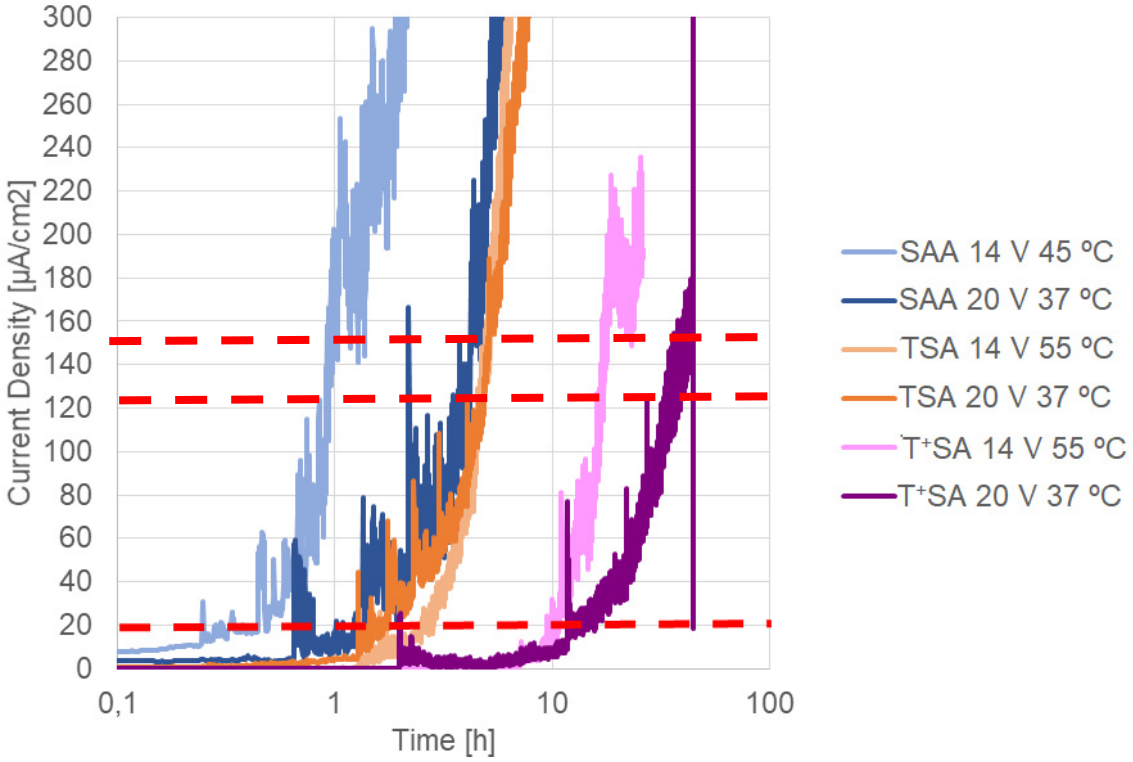


**Figure 8.** Evolution of current density of bare anodic oxide films in 3.5 wt.% NaCl polarised at 50 mV above the pitting potential of the substrate alloy.

### 3.2.2. Odd-Random-Phase Electrochemical Impedance Spectroscopy Degradation in an Acidified (pH 3) Dilute Harrison's Solution

Figure 9 shows a qualitatively representative example of an impedance spectrum obtained for one particular oxide after one hour immersion in the aggressive acidic solution. A measurement such as the one shown in Figure 9 is conducted every 20 min of immersion using a multi-sine excitation signal, as previously described in Section 2.7. In this way, it is possible to take 'snapshots' during the degradation of the anodic oxide in the acidic solution, ensuring that no further changes in the system are taking place during the measurement time, as often happens with single-sine EIS. In addition, measuring the noise, non-linearities, and non-stationarities in the system ensures the significance of the data measured and gives an insight into further details of the degradation process itself. The first thing to consider when analysing the output of an ORP-EIS measurement (e.g., Figure 9) is whether the noise/non-stationarities/non-linearities signals are of the same order of magnitude or even bigger than the impedance measured. Should this be the case, the impedance modulus should be carefully considered, as the signal to noise ratio would be very low. Furthermore, to interpret the non-linearities and non-stationarities signals, these must be first compared to the noise signal. If all three signals overlap, there are no non-linearities and/or non-stationarities taking place in the system.

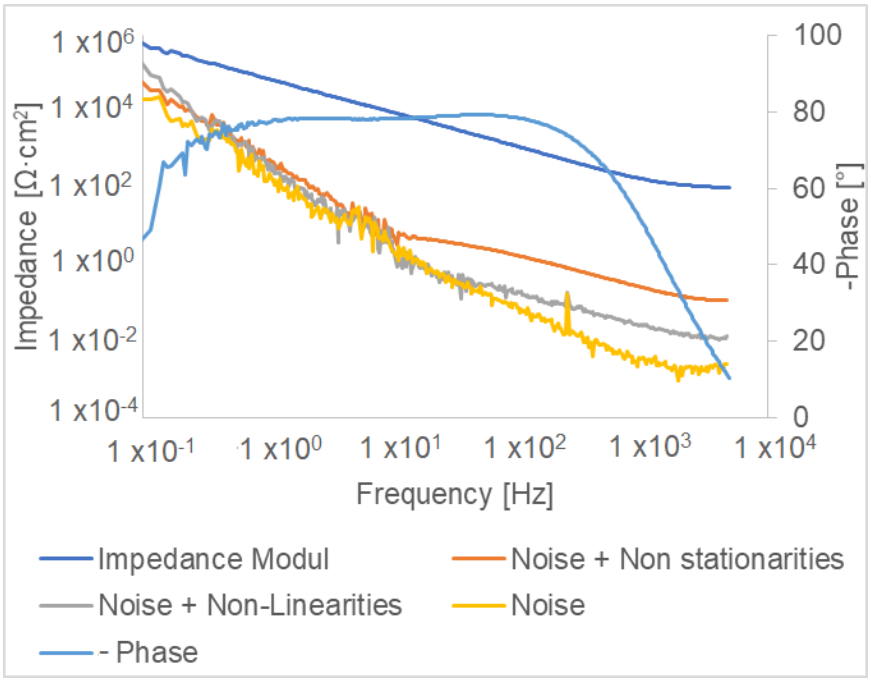


**Figure 9.** Example of ORP-EIS measurement. TSA 14 V 55 °C after one hour of immersion in acidic solution.

Qualitatively, as exemplified in Figure 9, all oxides show a marked non-stationary behaviour, and, to a lesser extent, a non-linear behaviour, in the mid to high frequency range (10 Hz to $10^4$ Hz in Figure 9) at a certain immersion time. To further analyse the evolution in time of the non-linear and non-stationary behaviour in the mid to high frequency range, the signals corresponding to the stochastic noise, the noise and non-linearities and the noise and non-stationarities at 100 Hz have been plotted in the time domain in Figure 10 for each anodic oxide under investigation. SAA oxides show high levels of non-stationarities from the first stages of immersion that tend to stabilise towards the end of the immersion. TSA and $T^+$SA oxides also show non-stationary behaviour that noticeably increases at later stages of immersion (ca. 800 to 1200 min of immersion). Furthermore, the peak of non-stationary response is slightly delayed for those TSA oxides formed at higher voltages and lower electrolyte temperatures (right column in Figure 10). The later appearance of the high non-stationary activity of TSA and $T^+$SA oxides compared to SAA oxides, as well as the delay for oxides formed at 20 V and 37 °C, can be interpreted as an increased resistance to the aggressive and fast oxide dissolution process in the acidic solution.

To further analyse the degradation behaviour of the different anodic oxides under study, the evolution of the impedance modulus at 0.5 Hz with immersion time is plotted in Figure 11. This frequency was chosen as a representative low frequency to show the evolution of the barrier properties of the film during degradation, while still retaining a good signal to noise ratio. Figure 11 shows only one curve per oxide type; however, all measurements were replicated, yielding similar results.

In the case of SAA oxides, Figure 11 reveals that the impedance modulus at 0.5 Hz is already decreasing from the first minutes of immersion. Further on, the higher scatter in the data indicates a high surface activity. On the contrary, the impedance modulus at 0.5 Hz of TSA and $T^+$SA oxides shows a stable period, during which little to no decrease in the modulus takes place. This stability period lasts approximately 1000 min (more than 16 h).

The FE-SEM images obtained comparing TSA and SAA samples after 960 min of immersion in acidic solution (see Figure 12) further highlight the differences between SAA and TSA films. The micrograph shows substantial degradation of the SAA oxide film (trenches and holes in the oxide film marked in Figure 12a), whereas, for the TSA film, only

minor changes (e.g., wider porous structure) are observable. The holes observed in the SAA oxide have most likely to do with the defective sites of the anodic oxide film (e.g., due to the presence of surface impurities) that have been aggravated by the immersion in the acidic electrolyte.

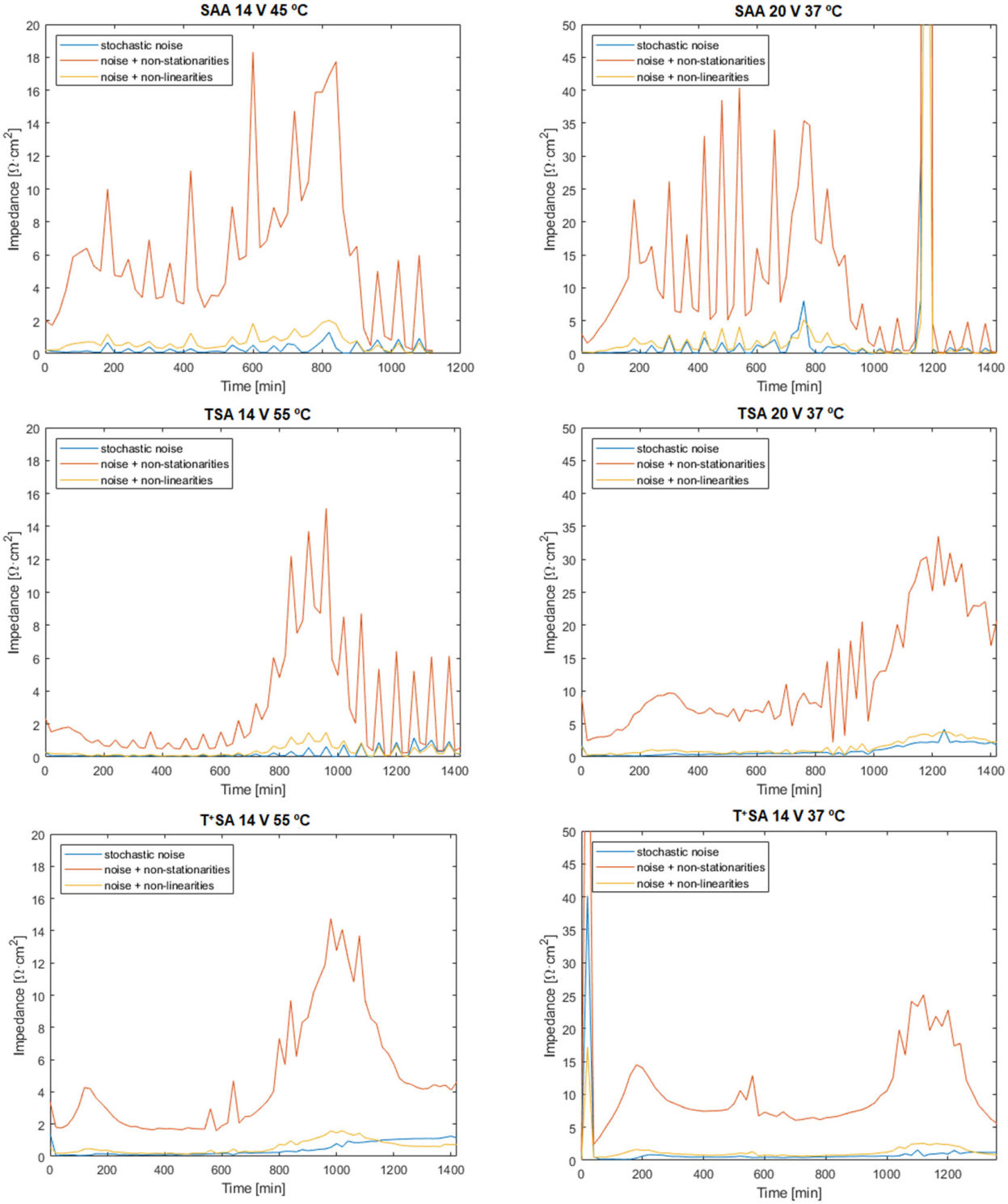


**Figure 10.** Noise, non-linearities, and non-stationarities measured at 100 Hz during immersion of the anodic oxide films in an acidified diluted Harrison solution by ORP-EIS.

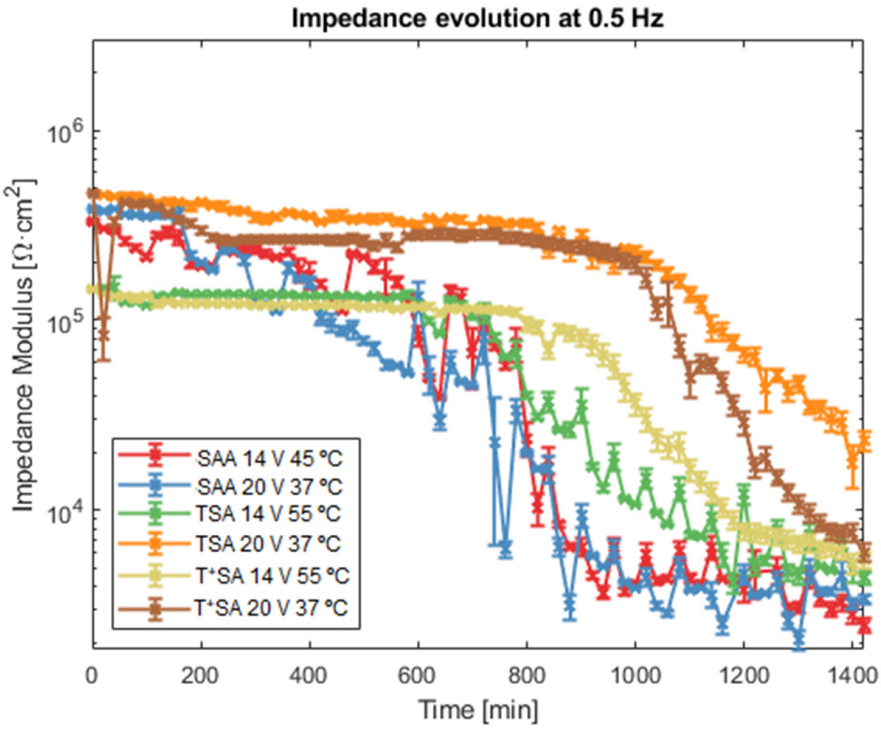


**Figure 11.** Evolution of the impedance of bare anodic oxide films at 0.5 Hz of different with immersion time in an acidified (pH 3) dilute Harrison's solution. Error bars represent the addition of stochastic noise and non-stationarities.

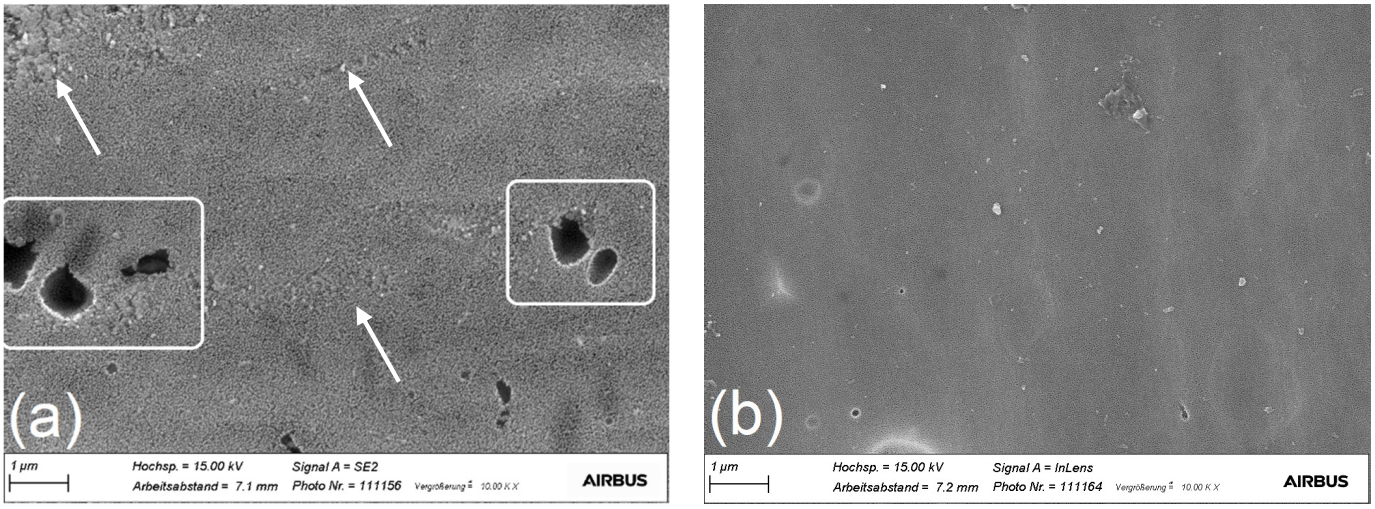


**Figure 12.** FE-SEM Images of (**a**) SAA 20 V 37 °C and (**b**) TSA 20 V 37 °C after 16 h of immersion in a pH 3 dilute Harrison's solution. The marked areas in figure (**a**) correspond to defects in the anodic film due to immersion in the aggressive acidic solution.

Degradation in an Alkalised (pH 10) Dilute Harrison's Solution

To study the degradation behaviour of the oxide films in alkaline solutions, the experiment was repeated in a dilute Harrison's solution adjusted to pH 10.

In the same way as the data presented before, Figure 13 shows the evolution of the impedance modulus at 0.5 Hz. Again, for better visualisation, only one data set per oxide is shown in Figure 13; however, all measurements were replicated, and similar results were obtained. Comparing Figure 11 to Figure 13, it is evident that the degradation process is much faster (nine times faster in average) and more aggressive in alkaline conditions than

in acidic conditions. In this case, regardless of the studied anodic oxide film, a very limited or no stability period at all is observed, and degradation takes place from the first instants of immersion. However, the rate at which the impedance modulus decreases is not the same for all oxides. Again, the impedance modulus decrease is sharper for SAA oxides (red and blue curves in Figure 13) compared to TSA and T$^{+}$SA oxides.

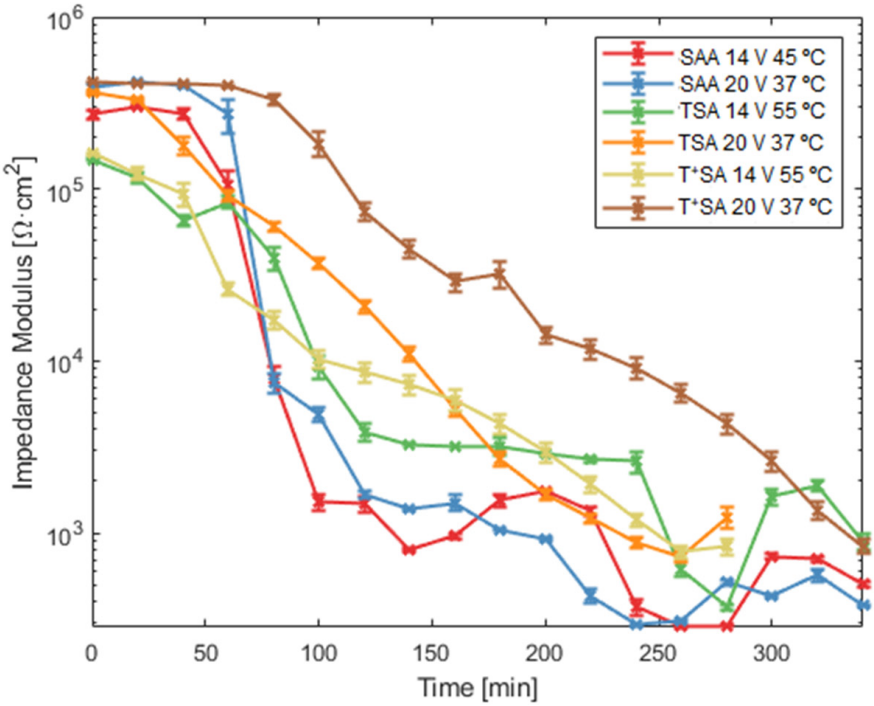


**Figure 13.** Evolution of the impedance at 0.5 Hz of different with immersion time in an alkalised (pH 10) dilute Harrison's solution. Error bars represent the addition of stochastic noise and non-stationarities.

### *3.3. Corrosion Protection Performance of Coated Anodic Oxide Films*

#### 3.3.1. Corrosion Protection in Neutral Salt Spray Test

Table 3 shows the average (over three panels) of the maximum paint creepage after 3000 h in a neutral salt spray test. As a general trend, the best results (smaller paint creepage length, smaller amount of corrosion spots) are obtained for the samples anodised at elevated temperatures. This is illustrated in Figure 14. On the contrary, no beneficial effect is observed by the presence of tartaric acid in the anodising electrolyte.

**Table 3.** Average length of maximum paint creepage of triplicate test and standard deviation after 3000 h exposure to the neutral salt spray test.

| Exposure Time (h) | Paint Creepage | Anodising Parameters | | | | | |
|---|---|---|---|---|---|---|---|
| | | **SAA 14 V 45 °C** | **SAA 20 V 37 °C** | **TSA 14 V 55 °C** | **TSA 20 V 37 °C** | **T$^{+}$SA 14 V 55 °C** | **T$^{+}$SA 20 V 37 °C** |
| 3000 h | Length (mm) | 1.5 | 2.4 | 1.7 | 3.1 | 1.8 | 4.2 |
| | SD (mm) | 0.1 | 0.6 | 0.6 | 0.8 | 0.5 | 0.4 |

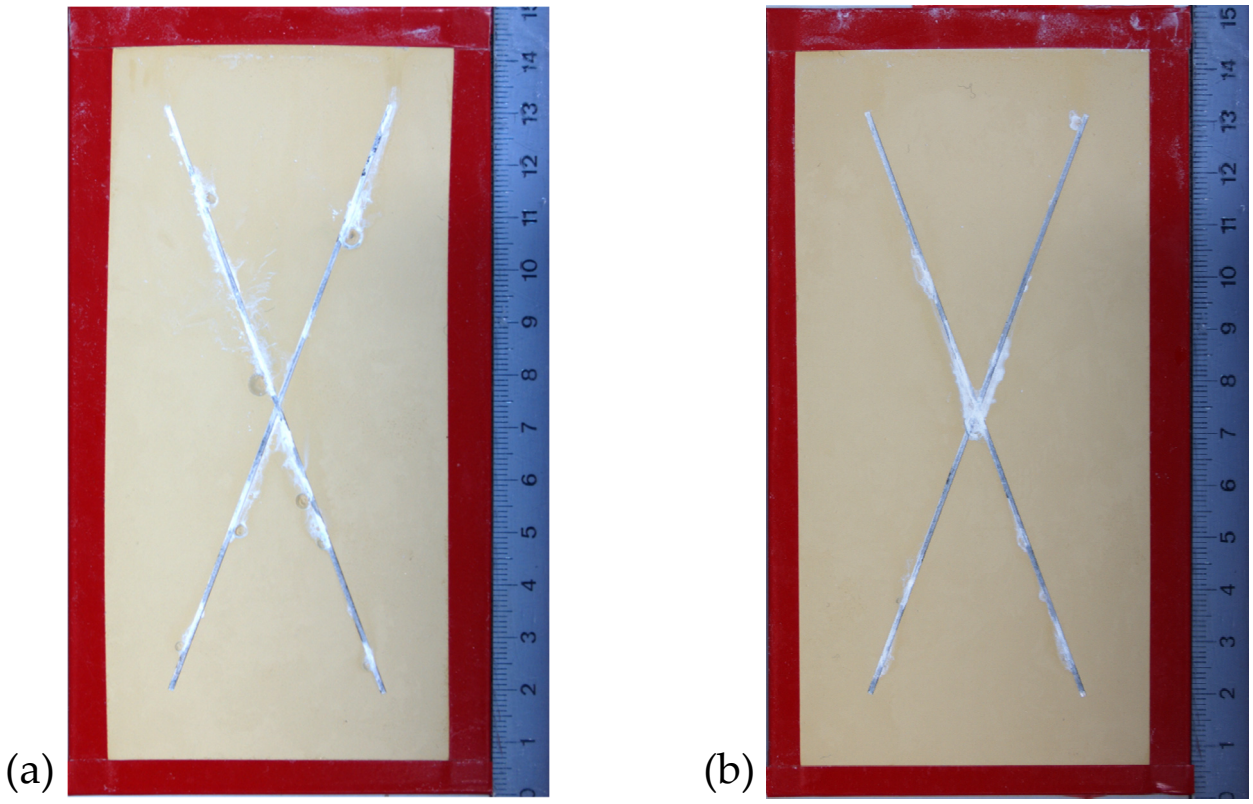


**Figure 14.** Visual inspection after 3000 h neutral salt spray test: (**a**) TSA 20 V 37 °C; (**b**) TSA 14 V 55 °C.

#### 3.3.2. Corrosion Protection Performance in a Filiform Corrosion Test

The filiform corrosion test is typically assessed by measuring the five longest filaments per test panel and averaging the results. The results obtained by this principle, considering three panels per anodising condition at the different inspection times during the 1000 h filiform corrosion test, are shown in Table 4. These results show similar filament lengths for all test panels, regardless of the anodising process parameters used.

**Table 4.** Summary of filiform corrosion test results.

| Exposure Time (h) | Filament | Anodising Parameters | | | | | |
|---|---|---|---|---|---|---|---|
| | | **SAA 14 V 45 °C** | **SAA 20 V 37 °C** | **TSA 14 V 55 °C** | **TSA 20 V 37 °C** | **T⁺SA 14 V 55 °C** | **T⁺SA 20 V 37 °C** |
| 168 | Length (mm) | 0.6 | 0.8 | 0.6 | 0.7 | 0.7 | 0.7 |
| | SD (mm) | 0.1 | 0.1 | 0.1 | 0.2 | 0.2 | 0.2 |
| 336 | Length (mm) | 1.0 | 1.0 | 1.0 | 1.0 | 1.1 | 1.0 |
| | SD (mm) | 0.1 | 0.2 | 0.2 | 0.1 | 0.2 | 0.1 |
| 500 | Length (mm) | 1.0 | 1.1 | 1.0 | 1.1 | 1.2 | 1.1 |
| | SD (mm) | 0.1 | 0.2 | 0.2 | 0.1 | 0.2 | 0.2 |
| 750 | Length (mm) | 1.2 | 1.2 | 1.2 | 1.1 | 1.4 | 1.3 |
| | SD (mm) | 0.3 | 0.3 | 0.2 | 0.1 | 0.3 | 0.2 |
| 1000 | Length (mm) | 1.4 | 1.3 | 1.3 | 1.4 | 1.5 | 1.3 |
| | SD (mm) | 0.2 | 0.3 | 0.2 | 0.1 | 0.3 | 0.2 |
| | Area ($mm^{2)}$ | 4.8 | 5.6 | 3.9 | 5.7 | 5.2 | 6.5 |
| | SD ($mm^2$) | 0.8 | 1.0 | 0.9 | 1.3 | 1.2 | 1.7 |

However, while the filament length is similar, the appearance of the filaments is dependent on the anodising parameters, particularly on the anodising temperature. The filaments are significantly thinner for those samples anodised at higher electrolyte temperatures. This is exemplified in Figure 15. To better quantify this observation, the average filament area has been measured using an FFT scanner coupled with automated image processing software. The results obtained, summarized in the last two rows in Table 4, confirm the qualitative observation, showing smaller average filiform areas for those substrates anodised at elevated temperatures (45 °C or 55 °C).

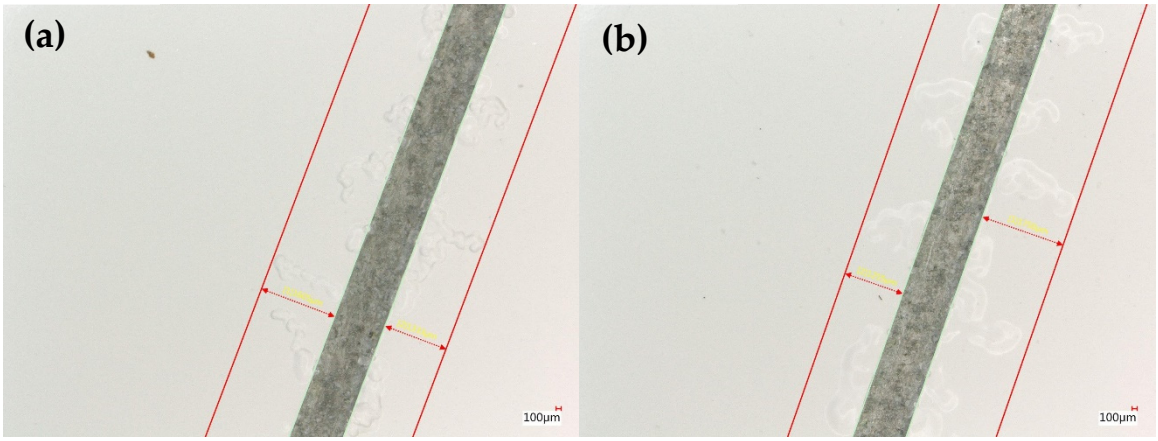


**Figure 15.** Comparison of filament appearance during FFT for (**a**) samples anodised at higher temperature and (**b**) samples anodised at lower temperatures.

### *3.4. Adhesion*

A cross-cut adhesion test [ISO2409] has been conducted to assess the adhesion properties of the anodic oxide films under study in combination with a Cr(VI)-free model primer in dry conditions and after two weeks of immersion in deionised water. All samples show good adhesion (see Table 5), with no failure at all or only small delamination (<5% of the total area of study) at the cutting intersections. This is the case regardless of the anodising electrolyte used. These results indicate that, even though the cross cut adhesion test is widely used for the assessment of coating adhesion, it is not sensitive enough to capture the differences in adhesion properties among anodic oxide films [33].

**Table 5.** Results of the cross-cut test for the Cr(VI)-free model primer in dry condition and after two weeks of immersion in deionised water.

| Anodising Parameters | Dry Adhesion | Wet Adhesion |
|---|---|---|
| SAA 14 V 45 °C | No failure | No failure |
| SAA 20 V 37 °C | No failure | No failure |
| TSA 14 V 55 °C | No failure | No failure |
| TSA 20 V 37 °C | No failure | Delamination <5% of area |
| $T^{+}$SA 14 V 55 °C | No failure | No failure |
| $T^{+}$SA 20 V 37 °C | No failure | Delamination <5% of area |

## 4. Discussion

### *4.1. The Role of Anodising Parameters on the Morphology and Chemistry of Anodic Oxide Films*

The morphological characterisation of the oxide films reveals an important influence of the electrolyte temperature in terms of porosity and ultimate surface roughness. The high anodising temperature condition leads to an enhanced oxide dissolution, especially in the uppermost area of the oxide, which is in contact with the anodising electrolyte for the entire anodising time [19,34]. As a consequence, the pore mouths are wider and even coalesce and, at the same time, the ultimate surface becomes rougher, in comparison to the narrow

pores and smooth surfaces seen on the oxides formed at a lower temperature. To a lesser extent, the electrolyte chemistry has also an effect on the porosity of the resulting oxide films, with SAA films showing higher porosity values at the surface of the anodic oxide. It has been previously reported that the addition of tartaric acid to a sulfuric acid electrolyte leads to a reduction in the dissolution reaction rate [23]. Hence, pore mouth widening through oxide dissolution is less significant in tartaric acid containing electrolytes. Finally, even though the formation voltage did not have a significant impact in the morphological analysis in this study and in a previous one by the same authors, it is widely accepted that the barrier layer thickness is proportional to the formation voltage [11,14]. Therefore, even though the barrier layer thickness has not been directly characterised in our study, it can be assumed that the barrier layer of the anodic oxide films formed at 20 V is thicker than for the oxides formed at 14 V.

In terms of oxide chemistry, no significant differences could be measured, neither by XPS nor by ToF-SIMS, regardless of the electrolyte chemistry, the formation voltage, and the anodising temperature. In particular no evidence of tartrate incorporation could be found.

### *4.2. The Role of Anodising Parameters on the Protective Properties of Bare Anodic Oxide Films*

The chronoamperometry results summarised in Figure 8 prove that the resistance to pitting behaviour of anodic oxide films formed in a tartaric acid containing electrolyte is better than for SAA oxides. This is derived from the fact that the time under galvanic stress until a significant rise in current density takes place is longer for TSA and $T^{+}SA$ oxides. This is in line with the results published by Vignoli et al. [24], where they compared anodic oxide films formed in chromic acid, sulfuric acid, and in several mixed sulfuric acid-organic acid electrolytes, among them tartaric acid. Furthermore, the present work demonstrates that, aside from the type of electrolyte, the pitting behaviour is also affected by the tartaric acid concentration, the electrolyte temperature, and the anodising voltage. In fact, increasing the concentration of tartaric acid substantially increases the time to pitting, while anodising at a lower temperature (37 vs. 55 °C) and at a higher voltage (20 vs. 14 V) slightly improves the pitting resistance of the resulting oxides.

The addition of tartaric acid to the anodising electrolyte also has a positive effect on the resistance of the anodic oxide film against dissolution, especially in the acidified corrosive solution and, to a certain extent, also in an alkaline environment. However, there is no clear trend correlating the electrolyte temperature and formation voltage with the resistance in the alkaline and acid corrosive solution.

Generally, the results obtained for the bare anodic oxides in terms of pitting resistance and stability in aggressive solutions are in good agreement with the improved corrosion properties of TSA vs. SAA oxides previously reported by many other researchers [23–25,28,29,32].

Taking into account the almost identical oxide chemical composition for all studied conditions, the differences in pitting susceptibility and pH stability among bare anodic oxide films must be attributed to their morphology.

The reduced porosity of TSA/$T^{+}SA$ oxide films is certainly contributing to its corrosion resistance, whereas the enhanced barrier properties due to a thicker barrier layer could be responsible for the trend of improved pitting resistance at higher formation voltages.

### *4.3. The Role of Anodising Parameters on the Corrosion Protection Performance of Coated Anodic Oxide Films*

Although the resistance of the bare anodic oxide films discussed in Section 4.2 provides a way of comparison between the different processes and may be relevant in a few particular applications, such as in practice, where anodic oxide films are typically covered by an organic coating loaded with corrosion inhibitors. Therefore, standard corrosion and adhesion tests of anodised and coated specimens have been performed.

In spite of the thicker barrier layer associated with a higher anodising voltage [9] and the higher pitting corrosion and acidic resistance reported in the present study for TSA and $T^{+}SA$ bare oxides, the corrosion test results (NSST in Table 3 and FFT in Table 4)

show better performance of the coated specimens that underwent higher temperature anodising processes (45 and 55 °C), regardless of the electrolyte chemistry and formation voltage. The wider pore mouths and rougher surface of the oxide films anodised at an elevated temperature (see Figures 4 and 5 and Table 2) promote mechanical interlocking and, consequently, adhesion. Therefore, it can be concluded that the enhanced stability at the coating/oxide interface plays a critical role in the NSST and FFT results. The correlation between the morphological features of anodic oxides obtained at elevated anodising temperatures and improved adhesion has been previously established in the literature [19,33].

## 5. Conclusions

The effect of the electrolyte chemistry, the electrolyte temperature, and the formation voltage on the resulting anodic oxide morphology and chemistry has been studied. The addition of tartaric acid to a sulfuric acid electrolyte leads to a slight reduction in porosity (from 7% for SAA 20 V 37 °C to 6% for TSA 20 V 37 °C). Wider pore mouths and dissolution driven roughness are the result of anodising at elevated temperatures, while the effect of the formation voltage on the characterised morphological features is not significant. The chemical composition of the surface of the anodic oxide films is almost identical, regardless of anodising parameters.

The resistance to pitting corrosion and the oxide degradation behaviour of bare anodic oxide films have been studied as a function of anodising parameters. The enhanced resistance against pitting corrosion (from less than 1 h for SAA 14 V 45 °C to more than 10 h for T$^+$SA 14 V 55 °C) and against degradation in acidic solutions (from no stability period for SAA to ca. 16 h of stability for TSA and T$^+$SA) of the bare oxides formed in the presence of tartaric acid highlight the benefits of mixed sulfuric-tartaric acid electrolyte anodising processes. Although the anodising temperature and formation voltage play a minor role in comparison to the tartaric acid concentration, a tendency towards better pitting resistance is observed if anodised at lower electrolyte temperatures and higher voltages.

Finally, in combination with a corrosion inhibiting organic coating, the corrosion protection performance is dominated by the anodising electrolyte temperature (average creepage length of 1.7 mm for TSA 14 V 55 °C compared to 3 mm for TSA 14 V 37 °C). At elevated temperatures, an optimal morphology for enhanced coating adhesion is created, whereas the effect of the anodising voltage and of the anodising electrolyte for coated anodic oxides is concealed by the effect of temperature.

**Supplementary Materials:** The following supporting information can be downloaded at: https://www.mdpi.com/article/10.3390/coatings12070908/s1, Figure S1: Detailed photoelectron peak for (a) C1s and (b) O1s; Figure S2: Example of fitted photoelectron peak for (a) C1s and (b) O1s; Figure S3: Depth profile of barrier oxide films. (a) SAA 14 V 45 °C; (b) TSA 14 V 55 °C. Concentration of C, F and S multiplied by 5; Figure S4: Detailed Spectra Porous Layer of (a) C1s; (b) O1s; (c) S2p; (d) F1s; Figure S5: ToF-SIMS spectra of $C_4H_5O_6^-$ molecular fragment measured on SAA, TSA and T$^+$SA barrier anodic oxides films formed at 37 °C; Figure S6: ToF-SIMS spectra of a protonated tartrate molecular fragment ($C_4H_5O_6^-$) (a) and (b) of an aluminum tartrate molecular fragment ($C_4H_5O_6Al^-$). Measured on SAA, TSA and T$^+$SA porous oxide films formed at 37 °C; Figure S7: ToF-SIMS spectra of $F^-$ molecular fragment. Measured on SAA, TSA and T$^+$SA porous oxide films formed at 37 °C; Table S1: Chemical composition measured by XPS on barrier oxide layers at 45° and 15° take-off angles; Table S2: Constraints applied for the curve fitting of the O1s and C1s photoelectron peaks as proposed by Abrahami et al.; Table S3: Atomic concentration and standard deviation calculated from three independent measurements of each deconvoluted chemical state in the C1s and O1s photoelectron peaks; Table S4: Chemical composition estimated from the detailed spectra of porous anodic oxide films. References [43–46] are cited in the Supplementary Materials.

**Author Contributions:** Chronoamperometry, FE-SEM, XPS, Corrosion and adhesion tests, M.P.M.-V.; ORP-EIS Measurements, M.D.H.; ToF-SIMS Characterisation, K.M.; Writing—original draft preparation, M.P.M.-V.; Writing—review and editing, S.T.A., H.T., T.H. and M.B.; Supervision, S.T.A., H.T., T.H. and M.B. All authors have read and agreed to the published version of the manuscript.

**Funding:** This research was funded by Airbus Central Research and Technology and Research foundation—Flanders (grant number I006220N).

**Institutional Review Board Statement:** Not applicable.

**Informed Consent Statement:** Not applicable.

**Data Availability Statement:** Data sharing is not applicable to this article.

**Conflicts of Interest:** The authors declare no conflict of interest.

## Abbreviations

| | |
|---|---|
| CAA | Chromic Acid Anodising |
| TSA | Tartaric-Sulfuric Acid Anodising |
| SAA | Sulfuric Acid Anodising |
| NSST | Salt Spray Test |
| FFT | Filiform Corrosion Test |
| $E_{pit}$ | Pitting potential |
| ORP-EIS | Odd Random Phase Electrochemical Impedance Spectroscopy |
| RMS | Root Mean Square |
| CC | Cross cut test |
| FE-SEM | Field Emission Scanning Electron Microscopy |
| XPS | X-Ray photoelectron spectroscopy |
| ToF-SIMS | Time of Flight Secondary Ion Mass Spectroscopy |

## References

1. Gialanella, S.; Malandruccolo, A. *Aerospace Alloys*; Springer International Publishing: Cham, Switzerland, 2019; Available online: https://books.google.de/books?id=via7DwAAQBAJ (accessed on 30 May 2022).
2. Campestrini, P.; van Westing, E.; van Rooijen, H.; de Wit, J. Relation between microstructural aspects of AA2024 and its corrosion behaviour investigated using AFM scanning potential technique. *Corros. Sci.* **2000**, *42*, 1853–1861. [CrossRef]
3. Ambat, R.; Davenport, A.; Scamans, G.M.; Afseth, A. Effect of iron-containing intermetallic particles on the corrosion behaviour of aluminium. *Corros. Sci.* **2006**, *48*, 3455–3471. [CrossRef]
4. Liu, Y.; Arenas, M.; Skeldon, P.; Thompson, G.; Bailey, P.; Noakes, T.; Habazaki, H.; Shimizu, K. Anodic behaviour of a model second phase: Al–20at.%Mg–20at.%Cu. *Corros. Sci.* **2006**, *48*, 1225–1248. [CrossRef]
5. Guillaumin, V.; Mankowski, G. Localized corrosion of 2024 T351 aluminium alloy in chloride media. *Corros. Sci.* **1998**, *41*, 421–438. [CrossRef]
6. Hughes, A.E.; Birbilis, N.; Mol, J.M.; Garcia, S.J.; Zhou, X.; Thompson, G.E. High Strength Al-Alloys: Microstructure, Corrosion and Principles of Protection. *Recent Trends Process. Degrad. Alum. Alloys* **2011**, *1*, 223–262. [CrossRef]
7. Boag, A.; Hughes, A.; Wilson, N.; Torpy, A.; MacRae, C.; Glenn, A.; Muster, T. How complex is the microstructure of AA2024-T3? *Corros. Sci.* **2009**, *51*, 1565–1568. [CrossRef]
8. Blohowiak, K.Y.; Osborne, J.H.; Seebergh, J.E. *Development and Implementation of Sol-Gel Coatings for Aerospace Applications*; SAE Mobilus: Warrendale, PA, USA, 2009. [CrossRef]
9. Becker, M. Chromate-free chemical conversion coatings for aluminum alloys. *Corros. Rev.* **2019**, *37*, 321–342. [CrossRef]
10. del Olmo, R.; Mohedano, M.; Visser, P.; Matykina, E.; Arrabal, R. Flash-PEO coatings loaded with corrosion inhibitors on AA2024. *Surf. Coat. Technol.* **2020**, *402*, 126317. [CrossRef]
11. Thompson, G.E. Porous anodic alumina: Fabrication, characterization and applications. *Thin Solid Film.* **1997**, *297*, 192–201. [CrossRef]
12. Sulka, G.D. Highly ordered anodic porous alumina formation by self-organized anodizing. In *Nanostructured Materials in Electrochemistry*; Eftekhari, A., Ed.; John Wiley & Sons: Hoboken, NJ, USA, 2008; pp. 1–116. [CrossRef]
13. Curioni, M.; Skeldon, P.; Thompson, G.E.; Ferguson, J. Graded Anodic Film Morphologies for Sustainable Exploitation of Aluminium Alloys in Aerospace. *Adv. Mater. Res.* **2008**, *38*, 48–55. [CrossRef]
14. Wernick, S.; Pinner, R. *Surface Treatment and Finishing of Aluminium and Its Alloys*, 4th ed.; Finishing Publications: Warrington, UK, 1972; Volume 1.
15. Martínez-Viademonte, M.P.; Abrahami, S.T.; Hack, T.; Burchardt, M.; Terryn, H. A Review on Anodizing of Aerospace Aluminum Alloys for Corrosion Protection. *Coatings* **2020**, *10*, 1106. [CrossRef]
16. Xu, Y.; Thompson, G.; Wood, G.; Bethune, B. Anion incorporation and migration during barrier film formation on aluminium. *Corros. Sci.* **1987**, *27*, 83–102. [CrossRef]
17. Abrahami, S.T.; Hauffman, T.; de Kok, J.M.; Mol, J.M.; Terryn, H. XPS Analysis of the Surface Chemistry and Interfacial Bonding of Barrier-Type Cr(VI)-Free Anodic Oxides. *J. Phys. Chem. C* **2015**, *119*, 19967–19975. [CrossRef]

18. Aerts, T.; Jorcin, J.-B.; De Graeve, I.; Terryn, H. Comparison between the influence of applied electrode and electrolyte temperatures on porous anodizing of aluminium. *Electrochim. Acta* **2010**, *55*, 3957–3965. [CrossRef]
19. Abrahami, S.T.; De Kok, J.M.M.; Gudla, V.C.; Ambat, R.; Terryn, H.; Mol, J.M.C. Interface strength and degradation of adhesively bonded porous aluminum oxides. *NPJ Mater. Degrad.* **2017**, *1*, 8. [CrossRef]
20. OSHA, T. *OSHA, Toxic and Hazardous Substances in Occupational Exposure to Hexavalent Chromium*; United States Department of Labor: Washington, DC, USA, 2006.
21. Regulation (EC) No 1907/2006 of the European Parliament and of the Council of 18 December 2006 Concerning the Registration, Evaluation, Authorisation and Restriction of Chemicals (REACH), Establishing a European Chemicals Agency, Amending Directive 1999/45/EC and Repealing Council Regulation (EEC) No 793/93 and Commission Regulation (EC) No 1488/94 as Well as Council Directive 76/769/EEC and Commission Directives 91/155/EEC, 93/67/EEC, 93/105/EC and 2000/21/EC. 2006. Available online: https://eur-lex.europa.eu/eli/reg/2006/1907/2020-04-28 (accessed on 30 May 2022).
22. Dattilo, A.; Tamiro, S.; Romano, C. Anodizing Process, with Low Environmental Impact, for a Woodpiece of Aluminum or Aluminum Alloys. U.S. Patent US20020157961A1, 31 October 2002.
23. Curioni, M.; Skeldon, P.; Koroleva, E.; Thompson, G.E.; Ferguson, J. Role of Tartaric Acid on the Anodizing and Corrosion Behavior of AA 2024 T3 Aluminum Alloy. *J. Electrochem. Soc.* **2009**, *156*, C147–C153. [CrossRef]
24. Machado, T.V.; Dick, P.A.; Knörnschild, G.H.; Dick, L.F. The effect of different carboxylic acids on the sulfuric acid anodizing of AA2024. *Surf. Coat. Technol.* **2019**, *383*, 125283. [CrossRef]
25. Marzocchi, V.; Iglesias-Rubianes, L.; Thompson, G.; Bellucci, F. The influence of tartaric acid additions on the anodizing behaviour of aa2024-t3 alloy in sulphuric acid. *Corros. Rev.* **2007**, *25*, 461–474. [CrossRef]
26. de Miera, M.S.; Curioni, M.; Skeldon, P.; Thompson, G. The behaviour of second phase particles during anodizing of aluminium alloys. *Corros. Sci.* **2010**, *52*, 2489–2497. [CrossRef]
27. Iglesias-Rubianes, L.; Garcia-Vergara, S.; Skeldon, P.; Thompson, G.; Ferguson, J.; Beneke, M. Cyclic oxidation processes during anodizing of Al–Cu alloys. *Electrochim. Acta* **2007**, *52*, 7148–7157. [CrossRef]
28. Boisier, G.; Pébère, N.; Druez, C.; Villatte, M.; Suel, S. FESEM and EIS Study of Sealed AA2024 T3 Anodized in Sulfuric Acid Electrolytes: Influence of Tartaric Acid. *J. Electrochem. Soc.* **2008**, *155*, C521–C529. [CrossRef]
29. Arenas, M.; Conde, A.; de Damborenea, J. Effect of acid traces on hydrothermal sealing of anodising layers on 2024 aluminium alloy. *Electrochim. Acta* **2010**, *55*, 8704–8708. [CrossRef]
30. Wang, R.; Wang, L.; He, C.; Lu, M.; Sun, L. Studies on the sealing processes of corrosion resistant coatings formed on 2024 aluminium alloy with tartaric-sulfuric anodizing. *Surf. Coat. Technol.* **2018**, *360*, 369–375. [CrossRef]
31. Setianto, M.H.; Korda, A.A. Characterization of Tartaric-Sulphuric Acid Anodized 2024-T3 Aluminium Alloys with Anodizing Potential Variation. *J. Phys. Conf. Ser.* **2019**, *1204*, 012039. [CrossRef]
32. González-Rovira, L.; González-Souto, L.; Astola, P.J.; Bravo-Benítez, C.; Botana, F.J. Assessment of the corrosion resistance of self-ordered anodic aluminum oxide (AAO) obtained in tartaric-sulfuric acid (TSA). *Surf. Coat. Technol.* **2020**, *399*, 126131. [CrossRef]
33. Martinez-Viademonte, M.P.; Abrahami, S.T.; Hack, T.; Burchardt, M.; Terryn, H. Adhesion properties of tartaric sulfuric acid anodic films assessed by a fast and quantitative peel tape adhesion test. *Int. J. Adhes. Adhes.* **2022**, *116*, 103156. [CrossRef]
34. McCafferty, E. Sequence of steps in the pitting of aluminum by chloride ions. *Corros. Sci.* **2003**, *45*, 1421–1438. [CrossRef]
35. Van Gheem, E.; Pintelon, R.; Vereecken, J.; Schoukens, J.; Hubin, A.; Verboven, P.; Blajiev, O. Electrochemical impedance spectroscopy in the presence of non-linear distortions and non-stationary behaviour. *Electrochim. Acta* **2004**, *49*, 4753–4762. [CrossRef]
36. Breugelmans, T.; Lataire, J.; Muselle, T.; Tourwé, E.; Pintelon, R.; Hubin, A. Odd random phase multisine electrochemical impedance spectroscopy to quantify a non-stationary behaviour: Theory and validation by calculating an instantaneous impedance value. *Electrochim. Acta* **2012**, *76*, 375–382. [CrossRef]
37. Schoukens, J.; Pintelon, R.; Dobrowiecki, T. Linear modeling in the presence of nonlinear distortions. *IEEE Trans. Instrum. Meas.* **2002**, *51*, 786–792. [CrossRef]
38. Schoukens, J.; Pintelon, R.; Van Der Ouderaa, E.; Renneboog, J. Survey of excitation signals for FFT based signal analyzers. *IEEE Trans. Instrum. Meas.* **1988**, *37*, 342–352. [CrossRef]
39. *ISO 17872:2019*; Paint and Varnishes-Guidelines for the Introduction of Scribe Marks through Coatings on Metallic Panels for Corrosion Testing. International Organization for Standardization: Geneva, Switzerland, 2019.
40. *ISO 9227*; Corrosion Tests in Artificial Atmospheres: Salt Spray Tests. International Organization for Standardization: Geneva, Switzerland, 2017.
41. *DIN EN 3665*; Aerospace Series. Test Methods for Paints and Varnishes: Filiform Corrosion Resistance Test on Aluminium Alloys. Deutsches Institut für Normung e.V.: Berlin, Germany, 1997.
42. *ISO 2409*; Paints and Varnishes: Cross Cut Test. International Organization for Standardization: Geneva, Switzerland, 2013.
43. Carangelo, A.; Curioni, M.; Acquesta, A.; Monetta, T.; Bellucci, F. Cerium-based sealing of anodic films on AA2024T3: Effect of pore morphology on anticorrosion performance. *J. Electrochem. Soc.* **2016**, *163*, C907–C916. [CrossRef]
44. Elaish, R. Effects of fluoride ions in the growth of barrier-type films on aluminium. *Electrochim. Act.* **2017**, *245*, 854–862. [CrossRef]

45. Moulder, J.F.; Chastain, J. *Handbook of X-ray Photoelectron Spectroscopy: A Reference Book of Standard Spectra for Identification and Interpretation of XPS Data*; Physical Electronics Division, Perkin-Elmer Corporation: Waltham, MA, USA, 1992.
46. Limcharoen, A.; Pakpum, C.; Limsuwan, P. An X-ray Photoelectron Spectroscopy Investigation of Redeposition from Fluorine-based Plasma Etch on Magnetic Recording Slider Head Substrate. *Proc. Eng.* **2012**, *32*, 1043–1049. [CrossRef]